Blade and Rim Seal Design of a First Stage High Pressure Turbine for a 300 MWe Supercritical CO2 Power Cycle

Logan Tuite
Graduate Researcher
Purdue
West Lafayette, IN

Antoni Rebassa
Graduate Researcher
Purdue
West Lafayette, IN

Stephen Bean
Graduate Researcher
Purdue
West Lafayette, IN

Guillermo Paniagua
Prof. Mech Engineering
Purdue
West Lafayette, IN

Logan is a PhD candidate focusing on using scale-resolving simulations and experimental validation to characterize turbine blade and tip flow fluid dynamics in high Reynolds number and sCO2 flows

Antoni is a PhD student researching the dynamics of rim seal flow in sCO2 blades along with heat exchanger shape optimization and working with wind tunnel design for subsonic testing

Stephen graduated from Purdue with his Masters in Aerospace Engineering focusing on the development of squealer tip geometries for sCO2 flows

Guillermo is a professor of Mechanical Engineering focused on turbines, flow instabilities and measurement techniques

Abstract

A first stage high-pressure turbine (HPT) blade is optimized for a 300 MWe supercritical CO2 (sCO2) power cycle using the surrogate-assisted genetic algorithm optimizer in Numeca FINE/Design 3D with objectives of increasing efficiency and decreasing heat load to the blade. The National Institute of Standards and Technology Reference Fluid Thermodynamic and Transport Properties Database (NIST REFPROP) [1] data for supercritical CO2 is formatted into tables of bicubic polynomial coefficients for use in condensable gas simulations in FINE/Turbo. Nearly 3000 unique shapes are evaluated via three-dimensional Reynolds Averaged Navier Stokes simulations, yielding increases in efficiency of up to 0.85 percentage points and decreases in heat load of 14%. A final blade, deemed the advanced blade, is chosen for future experimental analysis. Following this, a squealer tip optimization is performed on both the baseline and advanced blade designs. This optimization resulted in a performance gain of 1.25 points in efficiency and 15% reduction in tip heat load compared to the baseline flat tip design at the same clearance. In tandem, an optimization of the rotor-stator platform rim seal is performed using a

parametrized geometry allowing for straight, meandering, and knife seal cavities. This multi-objective optimization focuses on decreasing the cooling mass flow and increasing the heat flux from the rotor and stator disk. The optimization resulted in cooling mass flow decreases of up to 26% while maintaining the average heat flux on the rim seal.

Nomenclature

BRASTA	Big Rig for Aerothermal Stationary Turbine Analysis
CADO	Computer Aided Design Optimization
HPT	High Pressure Turbine
L	Characteristic Length
LF	Leakage fraction
NIST	National Institute of Standards and Technology
PETAL	Purdue Experimental Turbine Aerothermal Laboratory
Q	Heat load
REFPROP	Reference Fluid Thermodynamic and Transport Properties
sCO2	Supercritical carbon dioxide
y+	Non-dimensional wall distance
$\dot{m}$	Mass flow
$\overline{Q}$	Average heat flux
η	Sealing Effectiveness
01	Vane Inlet Station
02	Blade Inlet Station
03	Blade Exit Station

1. Introduction

The in-depth aerothermal analysis of supercritical CO2 turbomachinery in literature is sparse. The investigation of compressor components, both numerically and experimentally is much more mature, with investigations such as the works of Zhang et al., Ameli et al., Rinaldi et al., Baltadjiev et al., Shuster, et al., and Dahlquist, et al. [2–7]; Dahlquist et al. [8] investigated the difference in profile losses expected from a design working in air and in sCO2, which is applicable to both compressor and turbine applications. Regarding axial turbine design, work such as that done by Senthil et al., Abdeldayem et al., and Shi et al. [9–11], has primarily been focused on overall architecture as opposed to an in depth analysis of the flow characteristics within a supercritical CO2 turbine blade.

In this work, a shape parametrization and numerical approach for the optimization of a first stage high pressure turbine blade for a supercritical CO2 power generation cycle are described, followed by a description of the unique features of the optimized families of blades. In order to test the blade geometries in the Big Rig for Aerothermal Stationary Turbine Analysis (BRASTA) at the Purdue Experimental Turbine Aerothermal Facility (PETAL) [12], a geometric and aerodynamic scaling analysis is presented to show the applicability of testing analogue to the design conditions in sCO2. As an integral part of this investigation, a squealer tip optimization is performed for both the baseline and advanced blade shapes, following from the work done by Andreoli et al. [13], where the outcome of the investigation is to be assessed experimentally using the same methods as designed for the blade experimentation.

The final aspect investigated is the optimization of the spacing between the stator and rotor disk. A small amount of sCO2 from the compressor is bypassed and fed to the turbine for cooling the hub disk, blades, and to prevent ingestion of the hot flow from the combustor. It is important to characterize this flow since it has been proven that it can produce changes in the degree of reaction of 11% [14], which directly affects the efficiency of the turbine blade; therefore it should be considered in the early stages of the design. The vanes and rotating blades create non-axisymmetric unsteady pressure fields in the passage that can lead to hot gas ingestion into the rim seal. This mechanism is known as externally induced ingress [15]. Additionally, the isolated effect of rotation can cause pressure in the wheel space to be lower than in the passage, leading to ingestion. This mechanism is known as rotationally induced ingress [16]. A computationally expensive, unsteady three-dimensional CFD would be required to accurately capture externally induced ingress, typically more prevalent in turbines. Since this work aims to optimize the rim seal geometry efficiently, the initial approach to designing the stator-rotor rim seal is based on a fundamental two-dimensional multi-objective optimization. A 3D model is constructed after the optimization to validate the 2D designs and compare two designs with a baseline, straight radial rim seal geometry.

2. Blade Design and Optimization

The basis of the blade parametrization is a trapezoidal blade with a hub to tip ratio of 0.953, and aspect ratio of 1.125, and a pitch to chord ratio of 1.05 operating at a total to static pressure ratio of 1.389 and a Reynolds number measured at the blade trailing edge of approximately 11 million. The inlet to the stage is nominally 303 bar and 1420 K of pure CO2. The blade is parametrized using five spanwise sections with parameters for each airfoil section as well as parameters for the overall blade. A surrogate-assissted genetic algorithm optimization scheme from MINAMO built into Numeca FINE/Design 3D [17] is used to create and analyze different blade shapes. Discussion regarding the domain setup, meshing, and grid convergence study can be found in [18]. The following sections discuss the procedure and outcomes of this part of the study.

2.1. Blade Parametrization

From a baseline configuration, the blade is parametrized for geometry perturbation by the optimizer to create new blade shapes. Figure 1 shows the parametrization of the blade overlayed on the final, advanced blade design.
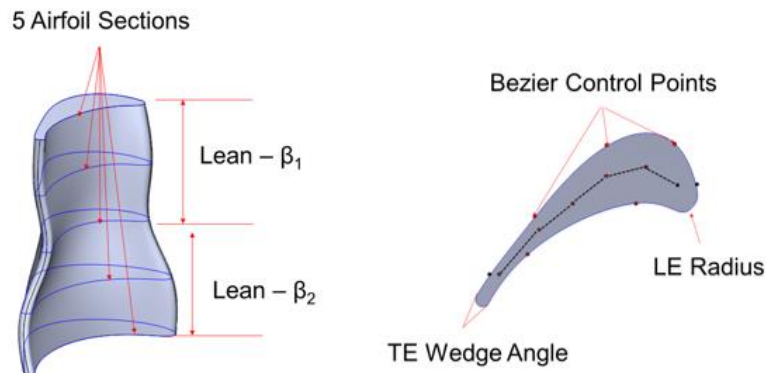

Figure 1: Blade parameters

The full blade is divided into five airfoil sections at five different spans (left), each described by suction side and pressure side Bezier curves, camberline B-spline, a leading edge radius, and a trailing edge wedge angle (right). The full blade itself has parameters, such as the lean from hub to midspan and the lean from midspan to tip. Overall, 70 parameters that describe the blade are allowed to vary during the optimization. The bounds of these parameters are initially set to +/- 10% from the nominal design, in accordance with the MINAMO recommendations from the FINE/Design 3D manual [17].

2.2. Blade Optimization

The blade optimization is a multi-objective optimization, which focuses on the reduction of heat load to the blade and the increase of blade efficiency, defined as the isothermal corrected efficiency given by Atkins and Ainsworth [19] and relayed in Equation 1.

$$\eta_{iso_{corr}} = \frac{T_q \omega + Q - T_{03}\left[\dfrac{2Q}{T_{02} + T_{03}}\right]}{\dot{m}[h_{01} - h_{03_{is}}]} \tag{1}$$

The results of the optimization are depicted in Figure 2. The left figure shows the design of experiments used to inform the optimizer initially, by randomly perturbing geometric features and analyzing blade shapes, as well as the first two evolutions of populations. In this case, it is readily seen that the optimizer quickly finds a minimum of heat load to the blade within the geometric confines available. To further the optimization, parameter bounds were relaxed from the initially instated +/- 10% to +/- 25%, resulting in the graph on the right of Figure 2, which further fills out the advancing front of the tradeoff between heat load to the blade and overall efficiency.
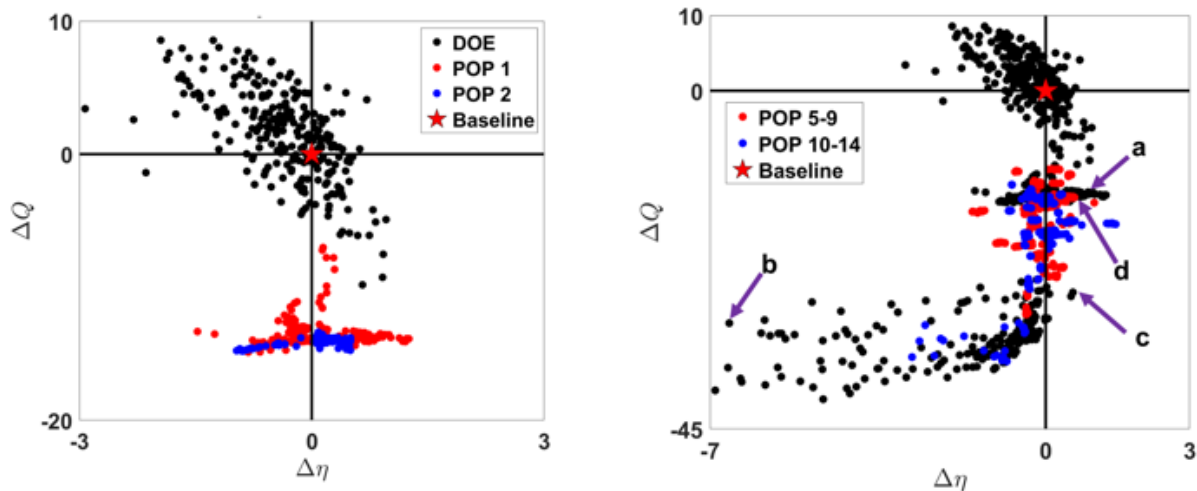

Figure 2: Blade Design Objective Graph Advancement

The relaxation of the parameter bounds allowed the optimizer to further fill out the space advancing towards a Pareto front, however many designs that heavily decreased the heat load were done so by simply reducing the overall blade area and were therefore not considered manufacturable. Those blades are the ones found in the lower left quadrant of the graph. To

combat this, a heavier weight was set on the increase of efficiency, even if the heat load were not reduced so much. This pushed the optimizer to find shapes, which more heavily populated the lower right quadrant, where both efficiency is increased and heat load is decreased. Those designs are portrayed in the right of Figure 2 by the red and blue points of populations 5-14.

2.3. Design Analysis

Nearly 3000 unique blade designs resulted from the optimization described above, and within these, three main high performing shape families are characterized, with one final advanced blade chosen for further experimental analysis and squealer tip optimization. Figure 3 shows representative blades of each of the three shape families in the top left and a comparison of the baseline and advanced blades in the bottom left ("a" being the baseline and "b" being the advanced blade"). The right of the figure shows an overlay of the isentropic loading and 2D blade profile at 15%, 50%, and 85% spans, for the baseline and advanced blades.
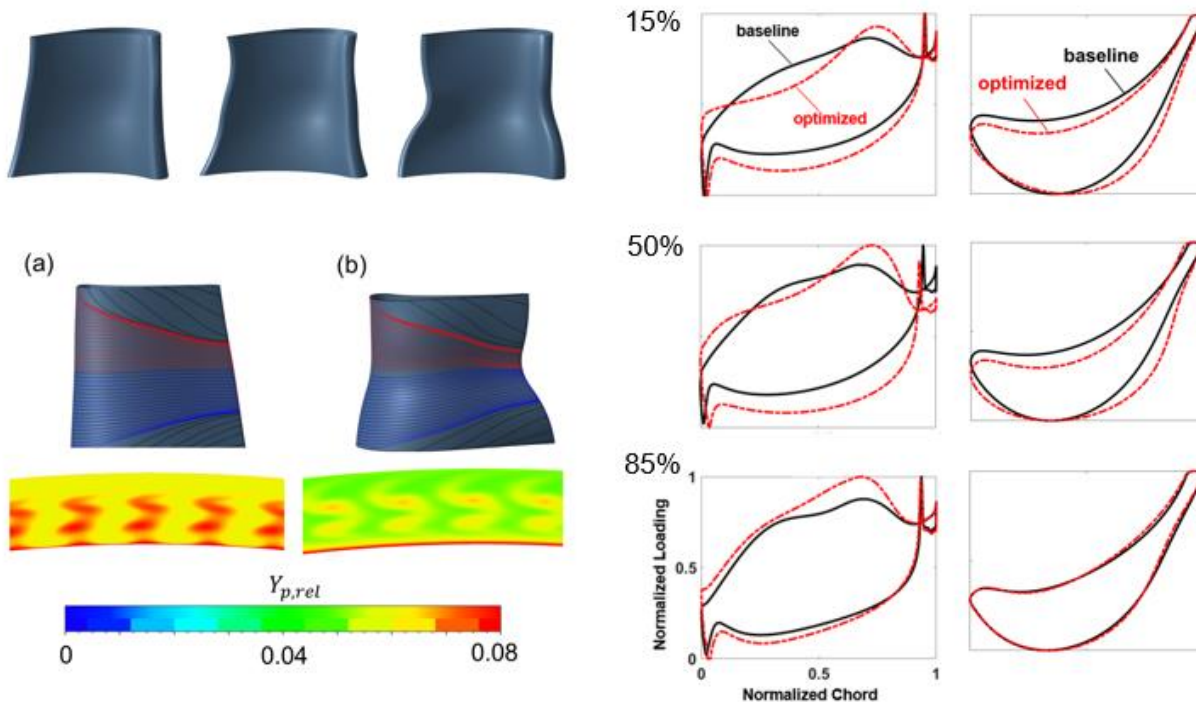

Figure 3: Blade design families and chosen advanced blade

The three shape families each have leading and trailing edge curvature in the spanwise direction, with the amount of curvature getting more aggressive as the geometry progresses. When comparing the three representative blades, the geometry progression chronologically through the optimization routine is from left to right; that is, the leftmost blade is the least altered from the baseline. Shapes such as this are created early in the optimization. The middle blade is towards the middle of the optimization, where the optimizer tends towards decreasing the heat load, and the rightmost blade is towards the later populations, where the optimizer is focused more heavily on increasing blade efficiency.

The comparison of the profile losses is included in the bottom left portion of Figure 3, where higher losses can be seen on the baseline blade compared to the advanced blade, and the high loss core in the advanced blade is more disconnected than in the baseline blade. Additionally, the loss at the hub is more uniform and does not penetrate as deeply into the freestream as in the advanced blade, where it almost meets with the high loss core. Overall, the advanced blade shows performance improvement over the baseline blade by improving the torque output with higher loading while staying within a 0.5% mass flow deviation from the design cycle.

2.4. Experimental Considerations

For the future experimental testing at PETAL in the BRASTA test section, consideration must be given to the difference in the working fluids. BRASTA is made to operate in an air environment, and the blade was designed numerically in an sCO2 environment. It is then prudent to make sure that the fluid dynamics seen in the design scale blade will also be realized in the test scale blade in air and that the performance gain will be comparable. Figure 4 shows a comparison of the blade outlet flow angle and pressure profiles (left) and the relative total pressure loss cores (right) for the blades in air and in sCO2.
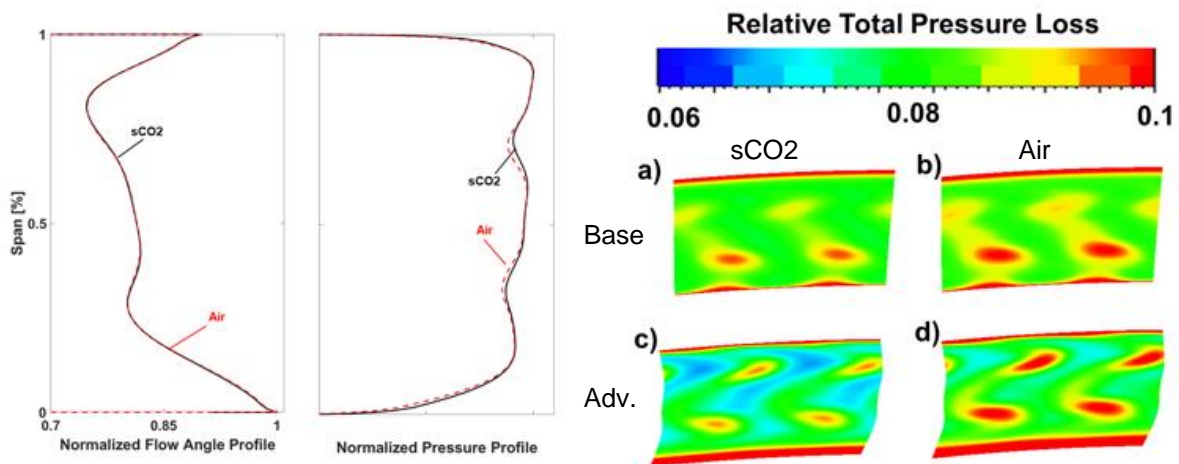

Figure 4: Influence of the working medium on outlet pressure and flow angle and relative total pressure loss

On the left of Figure 4, the radial profiles of flow angle and pressure profile are presented. If the development of the flow field is comparable between the two fluids, it is expected that the flow angle profile will stay the same and the pressure profile will have the same shape but a different magnitude. This latter statement follows from the work of Dahlquist et al., [8], where it is concluded that the profile losses in sCO2 should be less than for air at the same conditions. Therefore, less pressure deficit is expected in the sCO2 profile. This is revealed in the figure, as the sCO2 and air flow angle profiles (which are a result of the turning and are then also indicative of the loading on the airfoil) lie nearly on top of one another, lending credence to the fact that the change of medium does not affect the aerodynamic performance of the blade from a fundamental flow dynamics standpoint. The pressure profile is as expected, where there are pressure deficits lining up with the secondary flow loss cores, and in the sCO2, the deficit is less than in air. Further, the right portion of Figure 4 shows the relative total pressure losses one axial chord downstream of

the blade. The subfigures "a" and "c" are the baseline blade in air ("a") and sCO2 ("c"), and subfigures "b" and "d" are the baseline blade in air ("b") and in sCO2 ("d"). This figure shows that both in the sCO2 and air medium, the advanced blade has lower total pressure losses than the baseline blade, and between the two mediums, both blades shows similar patterns of secondary flow loss cores, with only the intensity changing, as anticipated from the aforementioned analyses and the radial profile. All together, this analysis provokes confidence in the ability to test the designs in an air facility at representative conditions and be able to show design improvement between blade shapes.

3. Tip Design

Careful design of a squealer tip geometry is crucial to recouping some of the losses introduced by the existence of a tip gap in a turbine rotor. The design of the squealer tip in this investigation follows from the work of Andreoli et al. [13], where arbitrary Bezier surfaces are generated via inputs from a multi-objective genetic algorithm optimizer, CADO [20] and applied to the specific tip geometry of the HPT blade. For this investigation, both the baseline and advanced blade run through the optimization process, with each being benchmarked with respect to the blade shape with a simple squealer.

3.1. Tip Parametrization

The parametrization of the tip is performed by defining a 5x5 matrix of control points in the range [0,1] that produce a cubic Bezier surface, upon which a threshold is set to create arbitrary splines that are mapped to the blade geometry Figure 5 shows the generation of a Bezier surface in 3D.
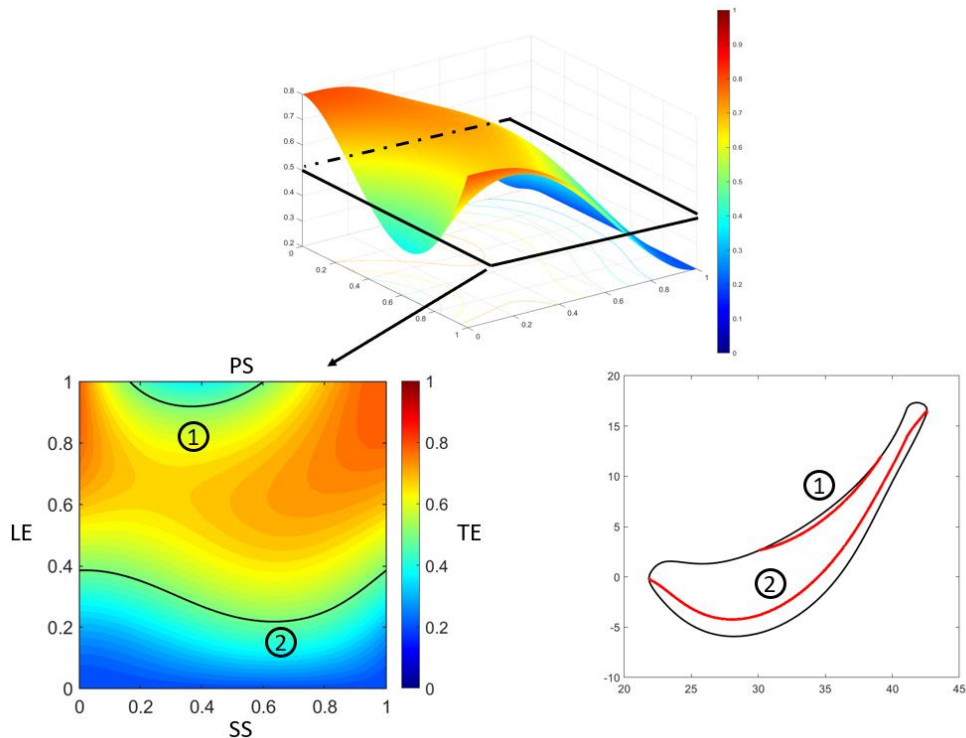

Figure 5: Tip Geometry Mapping

The threshold is set at 0.51, which corresponds to taking a plane slice at z = 0.51, as depicted by the black outline in the top of Figure 5. The result of this thresholding is shown in the lower left figure, which is a top-down plane view, where the black lines labeled "1" and "2" represent where the z = 0.51 plane intersects with the Bezier surface. Those black curves are then mapped to the actual blade geometry in the lower right picture with the corresponding "1" and "2". The mapping is done by producing a mesh grid of equal size on the 1 x 1 Bezier square to the airfoil geometry. In this manner, each coordinate point (x,y) on the 2D plane slice has a position within the confines of the airfoil shape and can be directly mapped. Ultimately, the lines produced on the airfoil in the above figure are then thickened to a minimum design thickness and applied to a solid blade geometry, as shown in Figure 6.
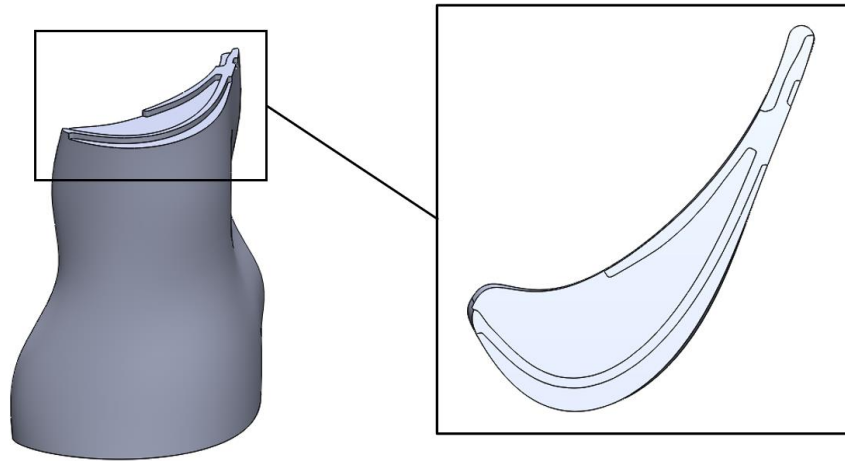

Figure 6: Tip profile on blade

3.2. Tip Optimization

The optimization follows from the generation of tip geometries from the parametrization process. The mapping of points and the airfoil tip shape stays the same throughout the optimization; the optimizer perturbes the inputs of the 5x5 control point matrix to generate different Bezier surfaces, which intersect with the z = 0.51 plane to generate different shapes. The rim shape points are output and geometry generated in IGG, where the geometry is output in an STL format to be read into HEXPRESS and mated to the blade to create a fluid domain to be analyzed using the unstructured solver, Numeca FINE/Open. The objective functions are the same as in the blade optimization presented in Section 2 – maximize the isothermal corrected efficiency and minimize the heat load to the tip.

3.3. Blade Shape Comparison

The optimization process is performed for both the baseline and the advanced blade in order to show a comparison of the performance of particular geometries on different blade shapes. The results are shown in Figure 7.
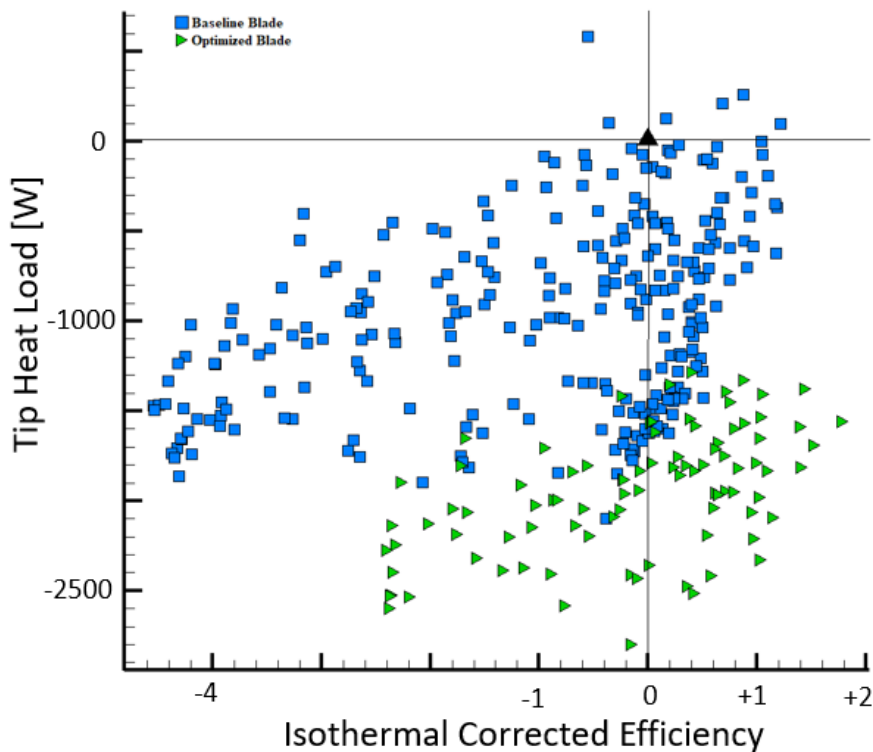
Figure 7: Comparison of tip geometry performance on different blade shapes

In Figure 7, the black triangle represents the baseline blade with a simple squealer rim geometry that goes around the entire outside of the blade tip. In general, the tip geometries that performed well on the baseline blade geometry performed well on the advanced blade geometry. This suggests that the difference in performance of an individual squealer tip geometry may not be as strong a function of the 2D tip airfoil shape as much as the global blade parameters – e.g. aspect ratio, pitch to chord ratio, hub to tip ratio, etc., which heavily influence the flow phenomena through the passage. Finally, the vertical shift between the baseline (blue) and advanced (green) markers is expected due to the fact that the advanced blade has a lower nominal heat load with a squealer than the baseline blade. Overall, the expected results of creating a better tip geometry on a better blade shape are realized by the green markers in the lower right quadrant, which denote increases in both objective functions better than what can be realized with the baseline blade shape.

4. Rim Seal Design

The stator-rotor platform cavity (rim seal) is an important area to focus on due to the necessity of cooling the hub disk and blades as well as to prevent ingress of hot gas from the primary flow path. The size and shape of the leakage flow path can drastically alter the performance of the entire blade, as a poorly designed rim seal can either cause a large ingress of the working fluid or can eject coolant far into the freestream and cause severe performance degradation to the

blade itself. This portion of the investigation focuses on finding shapes of the rim seal, which reduce the mass flow leakage while improving the cooling of the machine components surrounding the rim seal (rotor discs and bearings).

4.1. Two-dimensional optimization

The computational domain is sketched in Figure 8, where the boundary conditions are imposed in the stator reference frame.
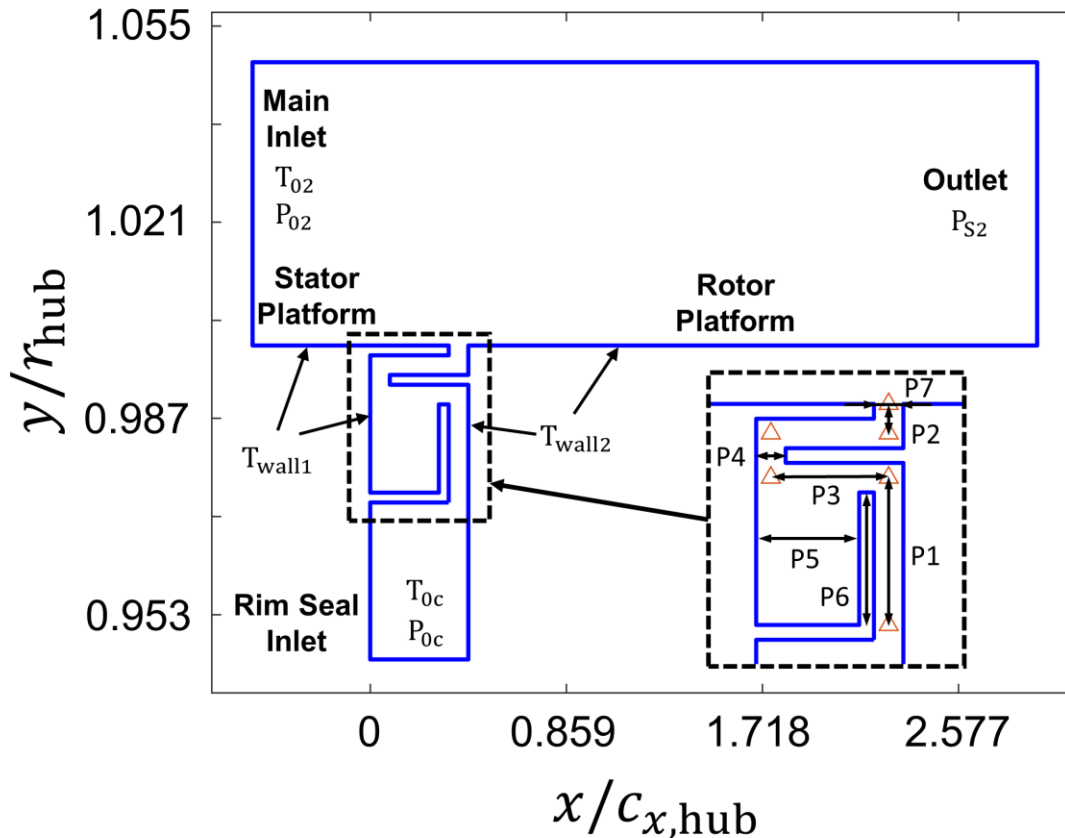

Figure 8. Parametrization and boundary conditions of the two-dimensional rim seal domain.

There are two inlets, one for the main passage and one for the rim seal, where total pressure and temperature are imposed. The static pressure at the outlet is set so that the Mach number in the domain is consistent with the demonstrator machine. Additionally, to simplify the computations further, the rotor rim seal wall and platform are stationary. To extract heat flux values, the walls are set to a no-slip isothermal condition. Seven parameters, sketched in Figure 8, are defined to allow the generation of geometries with knife-edge seals and recirculation cavities. Similar parametrizations were proposed by Moon et al. [21] based on the improvements shown experimentally by Popovíc et al. [22]. The parametrization constrains the geometry such that every design maintains a minimum axial distance of 2 mm between the walls and a minimum metal thickness of 1 mm.

The two functions used for the multi-objective optimization are:

$$F_1 = \min\left\{\frac{\dot{m}_{\text{seal,in}}}{\dot{m}_{\text{channel,in}}}\right\} = \min\{\text{LF}\} \qquad (2)$$

$$F_2 = \max\left\{\frac{Q_{\text{seal,stator}}}{L_{\text{seal,stator}}} + \frac{Q_{\text{seal,rotor}}}{L_{\text{seal,rotor}}}\right\} = \max\{\bar{Q}\} \qquad (3)$$

Where $\dot{m}_{\text{seal,in}}/\dot{m}_{\text{channel,in}}$, commonly defined in literature as leakage fraction (LF), is the ratio of the mass flow through the rim seal to the mass flow through the passage. Q is the heat transfer on the rim seal wall, and L is the length of the rim seal wall. The first objective, F_1, aims to minimize the bleed from the compressor, while the second objective, F_2, is meant to maximize the average heat flux from the stator and rotor walls of the rim seal to the fluid.

The sequence of processes shown in Figure 9a was followed to optimize the rim seal. The two-dimensional geometry is parametrized and generated in Matlab 2019; for CFD analysis, the domain is meshed with Numeca's unstructured mesher, HEXPRESS, and solved using Numeca FINE/Open. Supercritical CO2 gas tables from NIST REFPROP are coupled with the solver. After CFD analysis, the objective functions (Equations 2 and 3) are evaluated, and the results are fed back to a Genetic Algorithm Optimizer, CADO [20], where new geometries are determined based on the traits of the best-performing geometries.
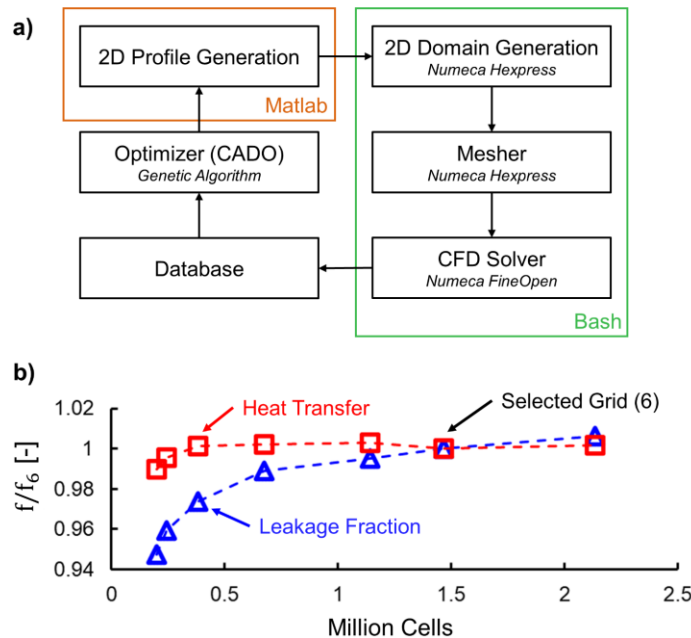

Figure 9. a) Flow chart for the rim seal optimization. b) Grid sensitivity of the two-dimensional model.

Before starting the optimization, a grid sensitivity analysis is performed with an axial rim seal geometry. Seven grids are generated with a number of cells ranging from 0.20 to 2.13 million. The grid size is uniformly increased in the x and y directions while keeping a constant first cell thickness of $5 \cdot 10^{-7}$ m. This results in a $y^+ < 1$, which leads to an accurate computation of heat flux. The two quantities of interest, leakage fraction and heat transfer are plotted as a fraction of the selected grid in Figure 9b. Grid number #6 is chosen since it balances accuracy and computational time well. The differences between the selected grid (#6) and the finest grid (#7) are 0.62% and 0.19% for the leakage fraction and heat transfer, respectively.

A full factorial design of experiments with 128 individuals is run to explore the design space. Following this, the genetic algorithm optimizer computed seven populations with 64 individuals, resulting in over 500 unique geometries evaluated to minimize bleed and maximize average heat flux. A plot of the Pareto Front defined by the objective functions is shown in Figure 10a. An axial rim seal is taken as the baseline reference. The tradeoff between both objective functions can be observed, where reducing the rim seal mass flow comes at the expense of a lower average heat flux from the walls to the fluid.
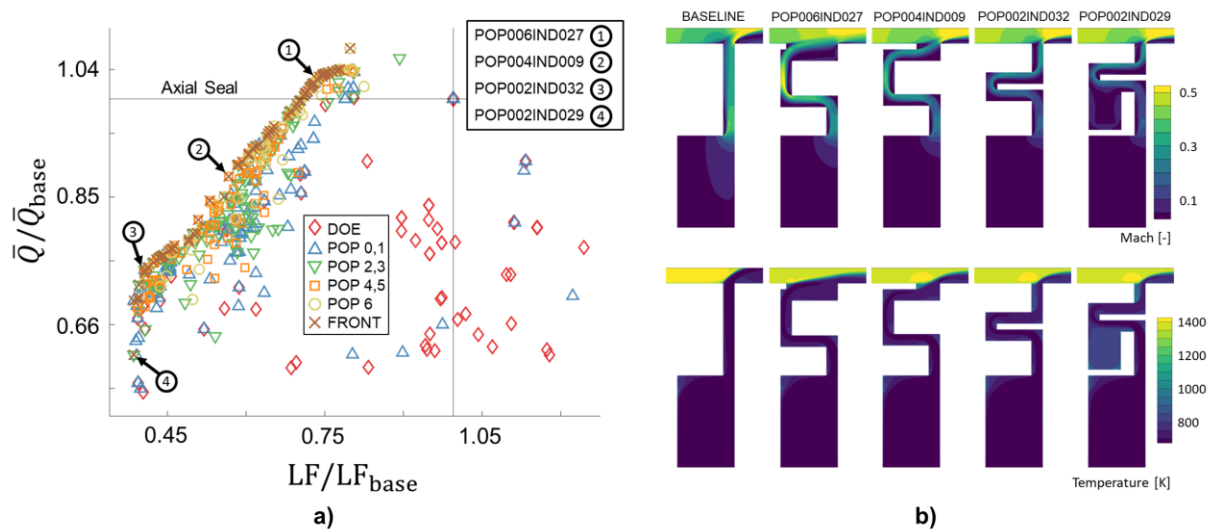

Figure 10. a) Pareto front with the design of experiment and populations. b)Temperature and Mach number contours of the analyzed geometries.

Table 1. Percent change in leakage fraction and average heat flux of 4 individuals with respect to the baseline.

INDIVIDUAL	% CHANGE LF	% CHANGE AVG. HF
POP006IND027	-26.124	2.9619
POP004IND009	-43.034	-11.536
POP002IND032	-59.094	-25.443
POP002IND029	-61.257	-38.083

Four individuals (1-4) are chosen for further aerothermal analysis. The percent change of the objective functions of these individuals with respect to the baseline is summarized in Table 1. The different geometries corresponding to the analyzed individuals, including the baseline, are shown in Figure 10b. Geometry 1 shows a decrease in leakage fraction of 26 % while maintaining a similar average heat flux, while the rest of the individuals present a large decrease in average heat flux and mass flow. These changes are achieved by two mechanisms: meandering and a change in exit area ratio. Geometry Number 4 presents a large decrease in average heat flux due to the large region of recirculating flow. Additionally, it is observed that an outlet area reduction leads to a smaller mass flow, and the lower velocity in the rim seal reduces the average heat flux. This two-dimensional analysis resulted in an extensive database used to determine the most influential parameters that should be kept for the three-dimensional rim seal.

4.2. Three-dimensional analysis

After generating an extensive database for two-dimensional cavities, evaluating the rim seal sealing effectiveness was necessary to validate the two-dimensional approach. The fluid domain with a summary of the boundary conditions is shown in Figure 11. The three-dimensional meshing and computations are performed in Ansys Fluent [23] while still using the NIST tables for sCO2. The vane is modeled so that the pressure field downstream allows the assessment of externally induced ingress. In these computations, no blades were implemented. Green and Turner [24] showed that the addition of blades caused a reduction in ingress compared to the case with only vanes. Therefore, sealing effectiveness would be underpredicted when only vanes are accounted for, ensuring that the leakage fraction chosen will prevent ingestion. The baseline, POP002IND029, and POP004IND009 geometries from the two-dimensional optimization are implemented.
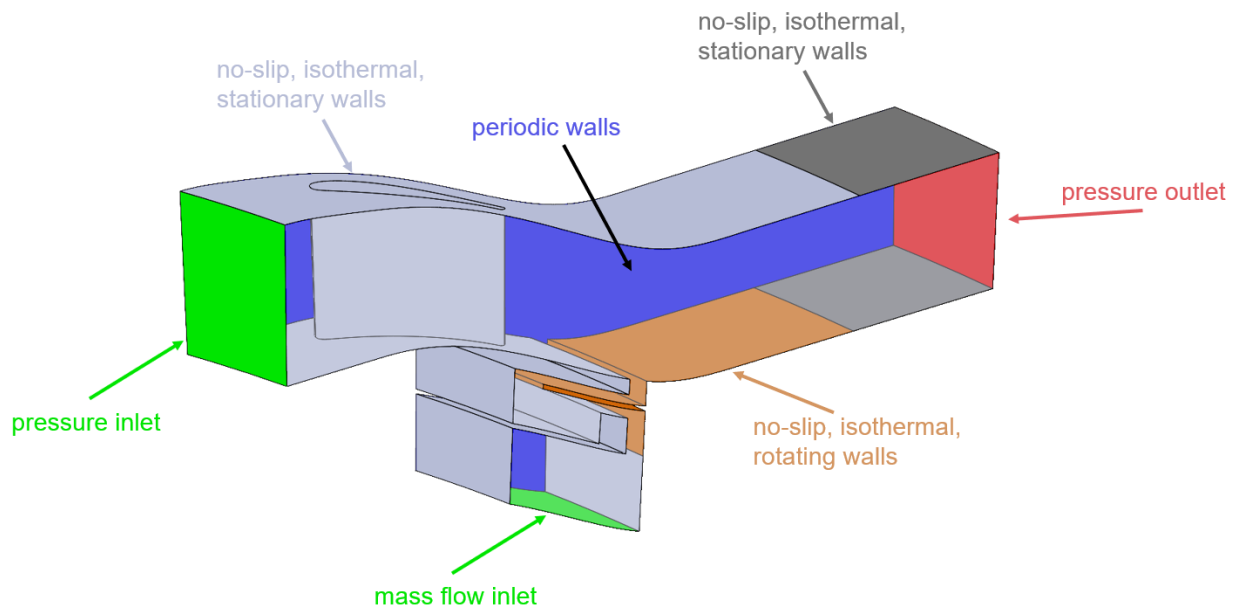

Figure 11. Three-dimensional computational domain.

The main parameter used to evaluate the performance of each of the cavities is the sealing effectiveness, defined as:

$$\eta(r) = \frac{T_{o,\text{passage, in}} - T_{o,\text{seal}}(r)}{T_{o,\text{passage, in}} - T_{o,\text{seal,in}}}$$

Where T_o is the area averaged total temperature. The mass flow through the rim seal is progressively changed in the CFD analysis, and the sealing effectiveness is evaluated 4 mm downstream of the plenum. The results for the axial seal and two of the optimized cavities (POP002IND029 and POP004IND009) are shown in Figure 12a. The rim seal walls are set to adiabatic for the sealing effectiveness computations. Additionally, the calculations are repeated for isothermal rim seal walls. The resulting heat transfer is plotted in Figure 12b. The new geometries present a substantial increase in sealing effectiveness as well as heat transfer on the rim seal walls. Increasing the mass flow to over a 0.5% leakage fraction yields an acceptable sealing effectiveness ($\bar{\eta} > 0.99$) for the three geometries.
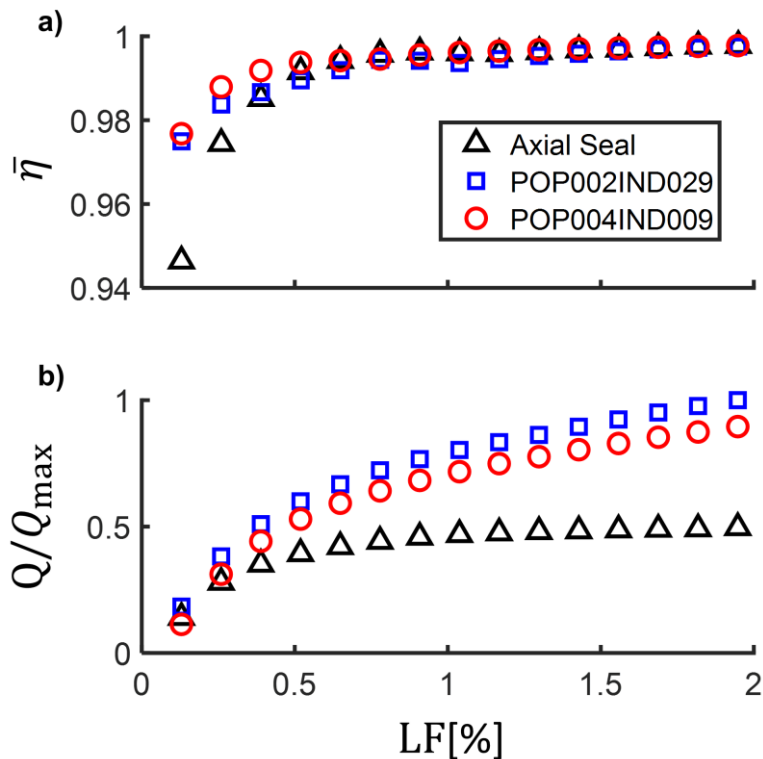

Figure 12. a) Circumferentially averaged sealing effectiveness 4 mm downstream of the rim seal plenum. b) Total Heat transfer on the rim seal walls.

5. Conclusions

The research presented in this paper has focused on the optimization and analysis of a first-stage high-pressure turbine blade designed for a 300 MWe supercritical CO2 power generation turbine. This comprehensive study was structured into three distinct yet interrelated parts: the initial design and analysis of the first-stage blade, the development of a squealer tip to mitigate tip losses, and the optimization and evaluation of the rim seal aimed at enhancing cooling efficiency while minimizing mass flow requirements. The findings from these investigations offer significant insights into turbine blade design and performance optimization in sCO2 environments and can be summarized as follows:

1. **Advanced Blade Design Efficiency**: The study demonstrates that an advanced blade design can maintain a mass flow deviation within a narrow margin of 0.5% from the cycle model. This precision in design translates to an increase in efficiency by 0.56 points and a substantial reduction in heat load by 12.4%. This achievement underscores the potential for fine-tuning blade designs to enhance turbine performance significantly.

2. **Air as a Testing Analog for sCO2**: The comparison between baseline and advanced blade designs tested in air provides a reliable analog for sCO2. It has demonstrated computationally that, under representative conditions, the aerodynamic behavior of downstream flows exhibits comparable characteristics in both air and sCO2 mediums. The observed deviations in profile losses are within expected ranges, bolstering the validity of using air for preliminary testing phases.

3. **Squealer Tip Geometry in sCO2 Environment**: The research further establishes the effectiveness of a squealer tip geometry in sCO2 conditions. This geometry reduces heat load at the blade tip and improves efficiency compared to standard squealer tip designs. The methodologies utilized here, adapted from previous air machine studies, demonstrate their applicability and effectiveness in the unique context of sCO2 turbines.

4. **Rim Seal Design and 2D Shape Optimization**: The innovative approach to rim seal design highlights the practicality and effectiveness of 2D shape optimization within sCO2 environments. The resulting geometries, which align closely with the outcomes anticipated in 3D analyses, offer a significant reduction in leakage fraction, up to 26%, while maintaining the average heat flux on the rim seal. This finding is pivotal, suggesting that 2D optimization strategies can effectively inform and guide more complex 3D design processes.

This paper contributes valuable advancements to turbine blade design and optimization, specifically in the context of supercritical CO2 power generation turbines. The results demonstrate the feasibility of achieving higher efficiency and reduced heat loads through meticulous blade and component design and opens avenues for further research and development in this burgeoning field of energy technology.

REFERENCES

[1]   Lemmon, E. W., Bell, I. H., Huber, M. L., and McLinden, M. O., 2018, "NIST Standard Reference Database 23: Reference Fluid Thermodynamic and Transport Properties-REFPROP, Version 10.0, National Institute of Standards and Technology."

[2]   Zhang, J., Gomes, P., Zangeneh, M., and Choo, B., 2017, *DESIGN OF A CENTRIFUGAL COMPRESSOR STAGE AND A RADIAL-INFLOW TURBINE STAGE FOR A SUPERCRITICAL CO 2 RECOMPRESSION BRAYTON CYCLE BY USING 3D INVERSE DESIGN METHOD.*

[3]   Ameli, A., Afzalifar, A., Turunen-Saaresti, T., and Backman, J., 2017, *EFFECTS OF REAL GAS MODEL ACCURACY AND OPERATING CONDITIONS ON SUPERCRITICAL CO2 COMPRESSOR PERFORMANCE AND FLOW FIELD.*

[4]   Rinaldi, E., Pecnik, R., and Colonna, P., 2015, "Computational Fluid Dynamic Simulation of a Supercritical CO2 Compressor Performance Map," J Eng Gas Turbine Power, **137**(7).

[5]   Baltadjiev, N. D., Lettieri, C., and Spakovszky, Z. S., 2015, "An Investigation of Real Gas Effects in Supercritical CO2 Centrifugal Compressors," J Turbomach, **137**(9).

[6]   Schuster, S., Benra, F.-K., and Brillert, D., *The 5 Th International Symposium-Supercritical CO2 Power Cycles Small Scale SCO2 Compressor Impeller Design Considering Real Fluid Conditions.*

[7]   Dahlquist, A., and Genrup, M., 2015, *Aerodynamic Gas Turbine Compressor Design for an Oxy-Fuel Combined Cycle.*

[8]   Dahlquist, A., Thern, M., and Genrup, M., 2014, *The Influence from the Working Medium on the Profile Loss in Compressor and Turbine Airfoils.*

[9]   Senthil Kumaran, R., Alone, D. B., and Kumar, P., 2020, *PROFILE LOSS INVESTIGATIONS WITH A S-CO2 AXIAL TURBINE AEROFOIL.*

[10]   Abdeldayem, A., White, M. T., and Sayma, A. I., *Comparison of CFD Predictions of Supercritical Carbon Dioxide Axial Flow Turbines Using a Number of Turbulence Models.*

[11]   Shi, D., Zhang, L., Xie, Y., and Zhang, D., 2019, "Aerodynamic Design and Off-Design Performance Analysis of a Multi-Stage S-CO 2 Axial Turbine Based on Solar Power Generation System," Applied Sciences (Switzerland), **9**(4).

[12]   Paniagua, G., Cuadrado, D., Saavedra, J., Andreoli, V., Meyer, T., Solano, J. P., Herrero, R., Meyer, S., and Lawrence, D., 2019, "Design of the Purdue Experimental Turbine Aerothermal Laboratory for Optical and Surface Aerothermal Measurements," J Eng Gas Turbine Power, **141**(1).

[13]   Andreoli, V., Braun, J., Paniagua, G., De Maesschalck, C., Bloxham, M., Cummings, W., and Langford, L., 2019, "Aerothermal Optimization of Fully Cooled Turbine Blade Tips," J Turbomach, **141**(6).

[14]   Paniagua, G., Dénos, R., and Almeida, S., 2004, "Effect of the Hub Endwall Cavity Flow on the Flow-Field of a Transonic High-Pressure Turbine," J Turbomach, **126**(4), pp. 578–586.

[15]   Owen, J. M., 2011, "Prediction of Ingestion through Turbine Rim Seals-Part II: Externally Induced and Combined Ingress," J Turbomach, **133**(3), pp. 31006-1-31006–9.

[16]   Owen, J. M., Zhou, K., Pountney, O., Wilson, M., and Lock, G., 2011, "Prediction of Ingress through Turbine Rim Seals-Part I: Externally Induced Ingress," J Turbomach, **134**(3).

[17]   NUMECA, 2021, "FINE/Design 3D User Manaul," Numeca International.

[18]   Tuite, L., Braun, J., and Paniagua, G., 2023, "Optimization of An HPT Blade and Sector-Based Annular Rig Design for Supercritical Co2 Power Cycle Representative Testing," J Eng Gas Turbine Power, pp. 1–15.

[19]   Atkins, N. R., and Ainsworth, R. W., 2012, "Turbine Aerodynamic Performance Measurement Under Nonadiabatic Conditions," J Turbomach, **134**(6).

[20]   Verstraete, T., *CADO: A Computer Aided Design and Optimization Tool for Turbomachinery Applications*.

[21]   Moon, M.-A., Lee, C.-S., Kim, K.-Y., and Kim, J.-H., 2014, *EFFECTS OF GEOMETRY ON SEALING EFFECTIVENESS OF A RIM SEAL*.

[22]   Popovíc, I., and Hodson, H. P., 2013, "Improving Turbine Stage Efficiency and Sealing Effectiveness through Modifications of the Rim Seal Geometry," J Turbomach, **135**(3).

[23]   ANSYS Inc., 2023, "ANSYS Fluent, Release 2023 R1."

[24]   Green, T., and Turner, A. B., 1994, "Ingestion Into the Upstream Wheelspace of an Axial Turbine Stage," J Turbomach, **116**(2), pp. 327–332.

ACKNOWLEDGEMENTS

DISCLAIMER

This report was prepared as an account of work sponsored by an agency of the United States Government. Neither the United States Government nor any agency thereof, nor any of their employees, makes any warranty, express or implied, or assumes any legal liability or responsibility for the accuracy, completeness, or usefulness of any information, apparatus, product, or process disclosed, or represents that its use would not infringe privately owned rights. Reference herein to any specific commercial product, process, or service by trade name, trademark, manufacturer, or otherwise does not necessarily constitute or imply its endorsement, recommendation, or favoring by the United States Government or any agency thereof. The views and opinions of authors expressed herein do not necessarily state or reflect those of the United States Government or any agency thereof.